

Ambilateral collimation study of the twin-jets in NGC 1052[★]

A.-K. Baczkó¹, E. Ros¹, M. Kadler², C. M. Fromm^{3,4,1}, B. Boccardi¹, M. Perucho^{5,6}, T. P. Krichbaum¹,
P. R. Burd², and J. A. Zensus¹

¹ Max-Planck-Institut für Radioastronomie, Auf dem Hügel 69, 53121 Bonn, Germany
e-mail: baczko@mpi-fr-bonn.mpg.de

² Institut für Theoretische Physik und Astrophysik, Univ. Würzburg, Emil-Fischer-Str. 31, 97074 Würzburg, Germany

³ Black Hole Initiative at Harvard University, 20 Garden Street, Cambridge, MA 02138, USA

⁴ Institut für Theoretische Physik, Goethe-Universität Frankfurt, Max-von-Laue-Straße 1, 60438 Frankfurt am Main, Germany

⁵ Dep. d'Astronomia i Astrofísica, Univ. de València, C/ Dr. Moliner 50, 46100 Burjassot, València, Spain

⁶ Observatori Astronòmic, Univ. de València, C/ Catedrático José Beltrán No. 2, 46980 Paterna, València, Spain

Received 29 July 2021 / Accepted 9 November 2021

ABSTRACT

Context. With the increase in the sensitivity and resolution of radio interferometry within recent years, the study of the collimation and acceleration region of extragalactic jets in active galactic nuclei (AGN) has come into focus. Whereas a large fraction of AGN jets show a change from parabolic to conical collimation profile around the Bondi radius, there is a small number of sources that display a deviation from this standard picture, including the radio galaxy NGC 1052.

Aims. We study the jet width profile, which provides valuable information about the interplay between the central engine and accretion disk system and the formation, acceleration, and collimation of the jets.

Methods. We observed the double-sided, low-radio-power active galaxy NGC 1052 at six frequencies with the VLBA in 2017 and at 22 GHz with RadioAstron in 2016. These data are combined with archival 15, 22, and 43 GHz multi-epoch VLBA observations. From ridge-line fitting we obtained width measurements along the jet and counter-jet which were fitted with single and broken power laws.

Results. We find a clear break point in the jet collimation profile at $\sim 10^4 R_S$ (Schwarzschild radii). Downstream of the break, the collimation is conical with a power-law index of 1.0–1.2 (cylindrical 0; parabolic 0.5; conical 1) for both jets. On the other hand, the upstream power-law index of 0.36 for the approaching jet is neither cylindrical nor parabolic, and the value of 0.16 for the receding jet suggests this latter is close-to cylindrical. For both jets we find a large opening angle of $\sim 30^\circ$ at a distance of $\sim 10^3 R_S$ and well-collimated structures with an opening angle of $< 10^\circ$ downstream of the break.

Conclusions. There are significant differences between the upstream collimation profiles of the approaching (eastern) and receding (western) jets. Absorption or scattering in the surrounding torus as well as an accretion wind may mimic a cylindrical profile. We need to increase the observing frequencies, which do not suffer from absorption, in order to find the true jet collimation profile upstream of $10^4 R_S$.

Key words. techniques: high angular resolution – galaxies: active – galaxies: jets

1. Introduction

The most prominent features of radio-loud active galactic nuclei (AGN; see e.g. Zensus 1997) are their relativistic jets (Blandford & Königl 1979). To unveil the physical processes behind their formation and evolution, radio astronomical studies have focused on imaging the region around the central engine by means of high-frequency observations. To investigate the jet-forming region requires high spatial resolution as well as precise knowledge of the location of the central engine. The most famous example is M 87. Its close distance and high-mass central supermassive black hole (SMBH) enabled imaging of the jet base very close to the central engine and its black hole shadow (EHT Collaboration 2019; Kim et al. 2018).

In recent years, extensive studies of the acceleration and collimation region revealed a transition from a parabolic to conical collimation at distances of $\sim 10^4$ – 10^6 Schwarzschild radii (R_S), where $R_S = 2GM_{\text{BH}}/c^2$. This is close to the gravita-

tional sphere of influence of the black hole for several sources, including ten nearby sources of the MOJAVE sample and M 87 (Kovalev et al. 2020; Asada & Nakamura 2012). There are several sources deviating from this standard picture. For example, in NGC 315 the transition is with $\sim 5 \times 10^3$ – $5 \times 10^4 R_S$ much closer to the central engine than the Bondi radius (Boccardi et al. 2021; Park et al. 2021). The high resolution provided by Very Long Baseline Interferometry (VLBI) at millimetre (mm) wavelengths (see Boccardi et al. 2017), in this case by the Global mm-VLBI array (GMVA), reveals very small transversal jet widths (e.g. M 87, Kim et al. 2018) and wide jet bases (e.g. Cyg A, 3C 84 Giovannini et al. 2018; Boccardi et al. 2016a). This suggests that jet launching through the ergosphere of the black hole and by the accretion disk play an important role in jet formation (Blandford & Payne 1982; Blandford & Znajek 1977).

In contrast to these sources, the twin jet in NGC 1052 (PKS B0238–084, MCG–01–07–034, J0241–0815) does not show a parabolic collimation region. However, recent findings are controversial. On the one hand, by fitting the jet width at multiple frequencies at single epochs, Nakahara et al. (2020) found a cylindrical collimation with a power-law index of $k = 0$ ($k = 0.5$: parabolic; $k = 1$: conical) at distances smaller than $10^4 R_S$, while

* FITS data of images are only available at the CDS via anonymous ftp to cdsarc.u-strasbg.fr (130.79.128.5) or via <http://cdsarc.u-strasbg.fr/viz-bin/cat/J/A+A/658/A119>

farther out the jets become conical. 3C 84 is the only other source with a similar collimation profile (Giovannini et al. 2018). On the other hand, based on a stacked 15 GHz Very-Long-Baseline Array (VLBA) image, Kovalev et al. (2020) found a power-law index closer to a parabolic collimation profile for the upstream jet of $k = 0.391 \pm 0.048$. In this paper, we combine single-epoch and stacked multi-frequency data of NGC 1052 in an attempt to solve the puzzle of the upstream collimation profile.

NGC 1052 is classified as a low-ionisation nuclear emission-line region object (LINER) based on its optical spectrum (Fosbury et al. 1978; Ho et al. 1997). It is located at a redshift of $z = 0.005037$ (assuming a systemic velocity of $v_{\text{sys}} = 1507 \text{ km s}^{-1}$; Jensen et al. 2003). Due to the close distance of the source, all our calculations are based on the redshift-independent distance of $D = 19.23 \pm 0.14 \text{ Mpc}$ (Tully et al. 2013), leading to a linear scale of $0.093 \text{ pc mas}^{-1}$. NGC 1052 hosts a SMBH with a mass of $10^{8.2} M_{\odot}$ (Woo & Urry 2002). Recently, a significantly lower mass of $10^{5.51} M_{\odot}$ was suggested assuming virialised Broad Line Region (BLR) movements (Kovalev et al. 2020). However, this method may be biased by optical obscuration of the central region. In addition, Kameno et al. (2020) infer a mass of $(2.13 \pm 0.09) \times 10^9 M_{\odot}$ inside the circumnuclear disk based on the measurement of the rotation curve of the circumnuclear disk. Considering this, and for consistency with our earlier work, we assume a mass of $10^{8.2} M_{\odot}$ throughout the paper.

NGC 1052 is one of the few sources revealing a double sided radio jet. The radio structure inside the optical galaxy spans over about 3 kpc and ends in diffuse lobes (Kadler et al. 2004a). At lower frequencies, the intrinsic total radio power of this galaxy is a factor of 10–100 lower than the radio power of FR I radio galaxies, such as M 87 and NGC 315 (with radio structures larger than 1 Mpc). In comparison to powerful FR II radio galaxies, such as Cygnus A, its radio power is even about 10^4 – 10^5 times lower. The symmetric radio jets in NGC 1052 are mildly relativistic ($\beta \lesssim 0.6$) in comparison to the highly relativistic jets in FR I and FR II radio galaxies. Based on several kinematic studies we adopt a viewing angle of $>80^\circ$ (Vermeulen et al. 2003; Böck 2012; Baczko et al. 2019). At centimetre wavelengths, a torus with an optical depth of $\tau_{1\text{GHz}} \sim 300$ to 1000 and a column density of 10^{22} cm^{-2} to 10^{24} cm^{-2} covers $\sim 0.1 \text{ pc}$ towards the eastern, approaching jet and $\sim 0.7 \text{ pc}$ towards the western, receding jet (Kameno et al. 2001; Vermeulen et al. 2003; Kadler et al. 2004a,b; Sawada-Satoh et al. 2008; Brenneman et al. 2009). This is consistent with a globally averaged column density of $(1\text{--}2) \times 10^{23} \text{ cm}^{-2}$ estimated from X-ray observations (Baloković et al. 2021). This results in an emission gap between both jet cores at frequencies below 43 GHz; see modelling by Fromm et al. (2018, 2019). At centimetre(cm)-wavelengths the mean speeds of features in both jets have been derived as $\beta \leq 0.39$ (Vermeulen et al. 2003; Böck 2012; Lister et al. 2019). Four years of 43 GHz VLBA observations revealed higher apparent velocities of $\beta_{\text{ej}} = 0.53 \pm 0.04$ and $\beta_{\text{wj}} = 0.34 \pm 0.04$ for the eastern and western jets, respectively, following an asymmetric evolution (Baczko et al. 2019). The jets were first detected at 86 GHz by the GMVA in 2004, revealing a nearly symmetric jet-counter-jet morphology with an unresolved central feature containing about 70% of the total flux density (Baczko et al. 2016).

In this paper, we focus on the collimation profile of NGC 1052 derived from quasi-simultaneous VLBI observations at frequencies from 1.5 GHz to 43 GHz. We combine the approaches by Nakahara et al. (2020) and Kovalev et al. (2020) in our analysis, in that we include quasi-simultaneous

multi-frequency observations and stacked images at 15, 22, and 43 GHz. The multi-frequency observations and their data reduction is presented in Sect. 2. In Sect. 3 we give an overview of the methods used to derive the physical quantities, which are further discussed in Sect. 4. Finally, in Sect. 5 we summarise our results and provide an outlook.

2. Observation and data reduction

The frequency-dependent free-free absorption of the jet emission in the torus blocks our view onto the inner jet regions of NGC 1052 at frequencies below 43 GHz (Kadler et al. 2004b). On the other hand, higher frequency observations cannot image the extended, optically thin emission of the outer jet. Therefore, in order to connect jet properties such as collimation and opening angle on parsec to milliparsec scales we observed NGC 1052 at multiple frequencies from 1.5 GHz up to 43 GHz with the VLBA and a global array joining the RadioAstron (RA) mission. In the following sections, we briefly summarise our individual observations, including data calibration and imaging.

2.1. Multi-frequency VLBA observations

We observed NGC 1052 with the VLBA at frequencies of 1.5, 5.0, 8.4, 15, 22, and 43 GHz on April 4, 2017. The data were recorded with the Roach Digital Backend (RDBE) at dual polarisation with eight sub-bands per polarisation band with a bandwidth of 32 MHz and a data rate of 2 Gbps. The correlation was performed at the National Radio Astronomy Observatory (NRAO) at the Array Operation Center of the VLBA in Socorro, NM, USA. In order to calibrate the NGC 1052 data the sources 0234+285, 3C 454.3, and 4C 39.25 were observed.

For calibration, we applied dedicated procedures for the VLBA within the Astronomical Image Processing System (AIPS; Greisen 1990). Delay and phase offsets between the single intermediate frequencies (IFs) were removed through fringe detection on a strong calibration source. In order to perform a priori amplitude correction, the task APCAL was applied using system temperatures provided by the array, which included corrections for the opacity. We performed global fringe fitting on all sources to solve for residual delays and rates. The calibrator source 3C 454.3 was used to correct for the bandpass shape over frequency bands. After these calibration steps, persistent offsets between IFs were corrected by an additional round of fringe fitting. To enhance the fringe detection, a preliminary image was produced in DIFMAP (Shepherd et al. 1994), which served as an input model for the (AIPS) FRING task while repeating the fringe-fitting procedure for NGC 1052. Following the calibration procedure, data were averaged over frequency for each IF. To ensure the same calibration routine for all frequencies, a Python script was applied, which automated the calibration process as much as possible. The script makes use of the PARSELTONGUE Python interface to AIPS (Kettenis et al. 2006).

Afterwards, the data were read into DIFMAP (Shepherd et al. 1994) for imaging and model fitting. Spurious data were flagged, followed by time averaging. Thanks to the use of preliminary images during the fringe detection in AIPS, the phases were sufficiently stable that we did not have to apply initial self calibration with a point-source model in DIFMAP. The final images (cf. Fig. 1) were produced using standard CLEAN and self-calibration steps for phase and amplitude. The image parameters for the naturally weighted maps are listed in Table 1.

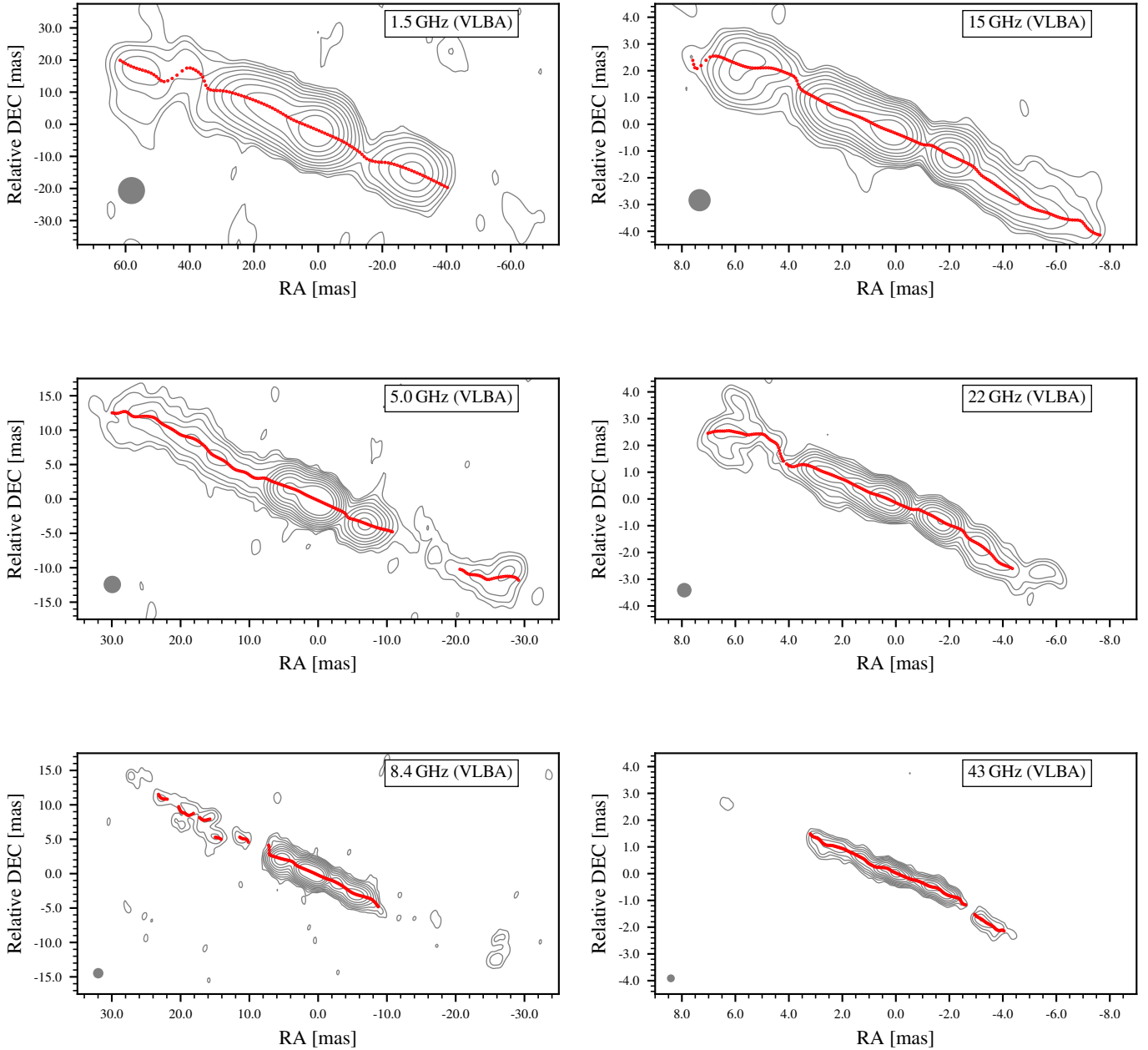


Fig. 1. Final clean image of VLBA observations at all six frequencies restored with a circular beam (calculated as $b = \sqrt{b_{\text{maj}} \times b_{\text{min}}}$ with the major and minor beam according to Cols. 7 and 8 of Table 1) with ridge lines plotted on top (red dots). The contours start at 4, 4, 4, 3, 2, and 3 times the noise level for 1.5, 5.0, 8.4, 15, 22, and 43 GHz (compare Table 1 Col. 3), respectively, and increase logarithmically by factors of two.

2.2. RadioAstron observation

On November 5, 2016, NGC 1052 was observed with the 10-m Space Radio Telescope (SRT) *Spekt-R* of the RadioAstron space-VLBI mission (Kardashev et al. 2012) and a large ground array consisting of antennas from the VLBA, Very Large Array (VLA), European VLBI Network (EVN), and the Long-Baseline Array (LBA) at 22 GHz. The participation of the Sardinia radio telescope, Effelsberg, Green Bank Telescope, and phased *Karl Jansky* Very Large Array added high-sensitivity dishes to the array. The correlation was performed at the DiFX software correlator in Bonn. The final set of telescopes was very heterogeneous, with different frequency setups. This resulted in different band widths and an inconsistent number of bands for individual telescopes. To allow correlation of the experiment

we used zoom-bands, which divides larger bands to match narrower bands and therefore produce a consistent frequency band width for all telescopes (Deller et al. 2011). We did not detect any significant fringes on baselines to the space antenna *Spekt-R* at the Bonn correlator. Additional attempts using the geodetic software package PIMA (Petrov et al. 2011) did not improve the correlation. This can be explained by either (1) the large gap of ~ 4 earth diameters between ground-ground and ground-space baselines which reduces the signal-to-noise ratio (S/N) of possible fringes or (2) the complex extended structure of NGC 1052 at 22 GHz at the projection angle sampled by the RadioAstron baselines, which might be resolved in space-ground baseline (cf. Fig. 2). Hence, the spatial scales sampled by the ground-ground baselines and the ground-space baselines are different. Therefore, solutions from the ground-ground fringe fitting cannot be

Table 1. Image parameters for all analysed VLBA observations from April 4, 2017, with natural weighting.

Array	ν [GHz]	rms ^(1a) [mJy/beam]	rms ^(1b) [mJy/beam]	S_{peak} ⁽²⁾ [Jy/beam]	S_{tot} ⁽³⁾ [Jy]	b_{maj} ⁽⁴⁾ [mas]	b_{min} ⁽⁵⁾ [mas]	PA ⁽⁶⁾ [°]	DR ⁽⁷⁾
VLBA	1.5	0.07	0.19	0.33	0.62	13.22	5.37	-5.9	1737:1
VLBA	5.0	0.05	0.08	0.48	1.04	3.89	1.65	-5.0	6000:1
VLBA	8.4	0.07	0.10	0.36	1.12	2.30	0.99	-5.0	3600:1
VLBA	15.3	0.06	0.08	0.25	0.82	1.26	0.55	-6.3	3125:1
VLBA	22.2	0.08	0.09	0.18	0.80	0.86	0.34	-5.0	2000:1
VLBA	43.1	0.10	0.10	0.15	0.59	0.45	0.19	-4.4	1500:1
RA-G ^(a)	22.3	0.04	0.04	0.11	0.42	0.44	0.39	44	1000:1

Notes. ⁽¹⁾(a) Root-mean-square (rms) noise level of image (b) rms inside a structure-free window far away from the source structure. ⁽²⁾Peak flux density. ⁽³⁾Total recovered flux density. ⁽⁴⁾-⁽⁶⁾Major and minor axes and major axis position angle of the restoring beam. ⁽⁷⁾Dynamic range: ratio between the map peak and the rms inside a structure-free window far away from the source structure. ^(a)RadioAstron ground-array image parameters.

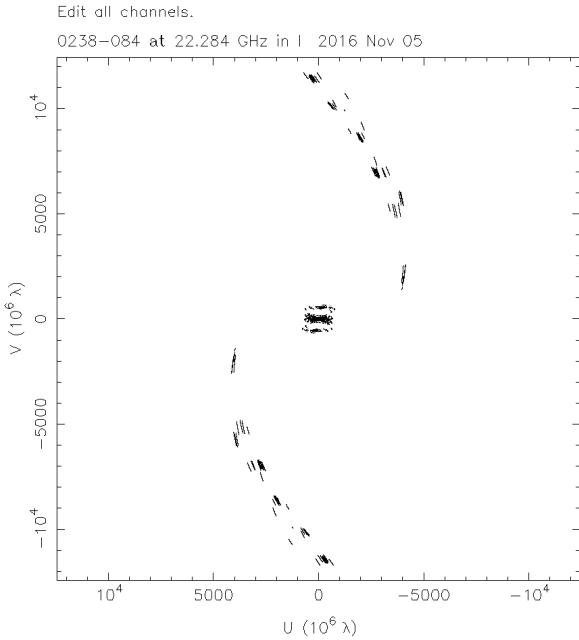


Fig. 2. (uv) coverage of the RadioAstron observation. We did not detect fringes on space-baselines.

applied to the long ground-space baselines. Also, fringe fitting directly on the ground-space baselines was not possible because of the very low S/N. The final correlator output therefore includes the RadioAstron data without delay correction and 29 antennas on the ground.

In order to calibrate this data set using AIPS, we followed a standard procedure similar to our approach described in Sect. 2.1 (following a standard approach as described in e.g. Vega-García et al. 2020). Because the array is large and heterogeneous, the calibration had to be planned with care not to lose any visibility data. The final correlation output revealed heterogeneous frequency coverage with a different number of IFs and only half the full bandwidth for a subset of antennas. In order to correct for atypical slopes and offsets in the visibility amplitude, we applied a bandpass calibration using the autocorrelated data. To improve the phase-calibration, a rough map of the data after an initial calibration served as an input model for an additional round of FRING for the target source NGC 1052.

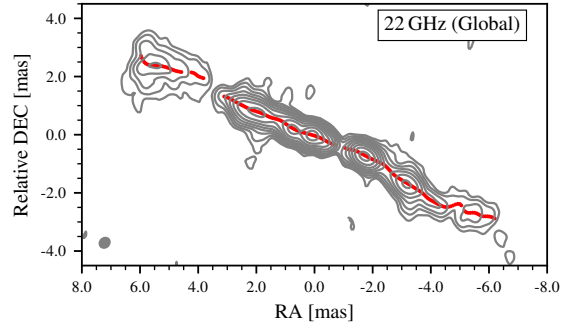


Fig. 3. Naturally weighted CLEAN contour map of RadioAstron observation of NGC 1052 at 22 GHz in November 2016, restored with a circular beam (calculated as $b = \sqrt{b_{\text{maj}} \times b_{\text{min}}}$ with the major and minor beam according to Cols. 7 and 8 of Table 1). The ridge-line is plotted on top (red dots). Contour lines begin at four times the noise level (compare with Table 1 Col. 3) and increase logarithmically by factors of two.

As a last step, the finally calibrated ground array and the rough image were used as input to attempt fringe detection on baselines to RadioAstron. However, at this stage, still no fringes were detected.

Thanks to the large ground array, this observation provides the highest resolution image at 22 GHz of NGC 1052 to date with a dynamic range of 1000:1. The inclusion of southern stations enhanced the north–south resolution with a nearly circular beam of 0.443×0.392 (mas) at a position angle of 44° . All parameters of the final CLEAN map are listed in Table 1. The final natural weighted clean map is shown in Fig. 3.

2.3. Stacked VLBA observations

In addition to the new VLBA and RadioAstron observations, we make use of four years of VLBA observations at 15 GHz, 22 GHz, and 43 GHz from 2005 to 2009 of NGC 1052, which have already been presented in Baczko et al. (2019) and Lister et al. (2019). To analyse the overall collimation profile along the twin jet, we produced stacked images at all three frequencies by restoring with a common circular beam of diameter $b = \sqrt{b_{\text{maj}} \times b_{\text{min}}}$. Based on the alignment presented in Baczko et al. (2019), the 22 GHz images were shifted with respect to the 43 GHz images before deriving the mean image. In the case of the archival 15 GHz data, the individual observations are not close enough to the 43 GHz or 22 GHz observations to align between frequencies. Assuming the centre of the gap between both jet cores is very close to the central 43 GHz peak, we aligned the 15 GHz images on this position before estimating the mean image. The stacked images are shown in Fig. 4 and their image parameters are listed in Table 2. The total flux density of the RadioAstron ground image is significantly lower than the VLBA-only image at the same frequency. This could be true variability, as NGC 1052 already showed strong variability in its total flux density within only a few months in previous observations. In addition, the RadioAstron observation suffered from several flux-scaling problems. Significant changes of the visibility amplitude over the IFs adds a large uncertainty on the total flux density scaling of the image.

3. Results

3.1. Image alignment of VLBA observations

We applied a 2D cross-correlation in Fourier space, pairwise at adjacent frequencies, in order to align all images (making

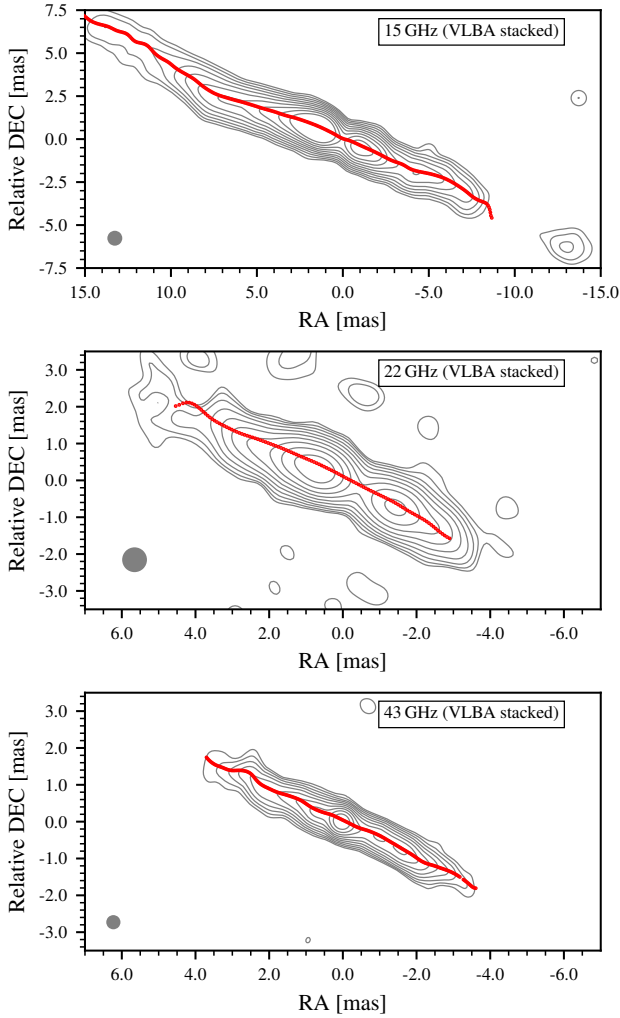


Fig. 4. Stacked images based on four years of VLBA observations at 15 GHz, 22 GHz, and 43 GHz (Baczko et al. 2019; Lister et al. 2019) restored with a circular beam. The ridge lines are plotted on top (red dots). The contours start at 0.5 times the noise level for 15 GHz, 22 GHz, and 43 GHz, which is derived as the mean rms from the individual images and increases logarithmically by a factor of two (compare Cols. 2 and 5 of Table 2).

Table 2. Image parameters for stacked VLBA maps.

ν [GHz]	rms ⁽¹⁾ [$\frac{\text{mJy}}{\text{beam}}$]	S_{peak} ⁽²⁾ [$\frac{\text{Jy}}{\text{beam}}$]	S_{tot} ⁽³⁾ [Jy]	beam ² [mas]
15	0.23	0.36	1.07	0.87
22	0.73	0.36	1.01	0.67
43	0.63	0.34	0.79	0.39

Notes. ⁽¹⁾The mean of the rms from all images used in the stacking. ⁽²⁾Circular beam FWHM equivalent to the median of the common circular beams for each image. ⁽³⁾Total recovered flux density.

use of the SCIKIT and EHTIM packages van der Walt et al. 2014; Chael et al. 2016, 2018). The images were produced by convolution of the CLEAN component delta functions with the natural restoring beam of the lower frequency image on a grid with the pixel size and field of view of the higher frequency image. This approach ensures that the cross-correlation is most sensitive for the source structure and not the noise. The free-free absorp-

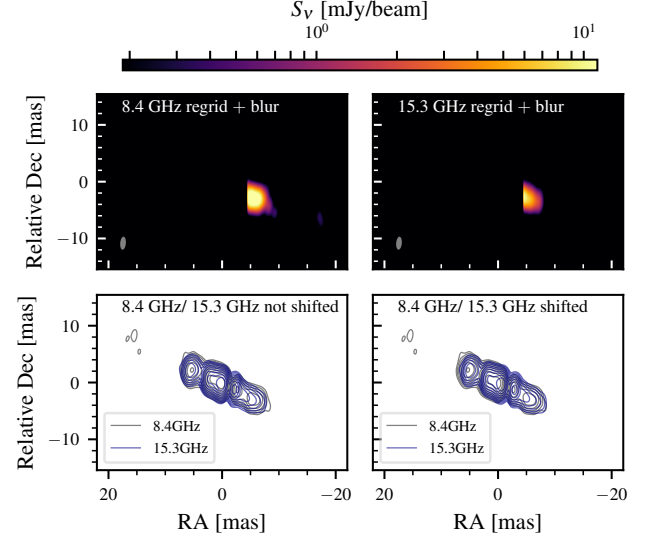


Fig. 5. One example of the alignment procedure of the VLBA images for the frequency pair 8.4 and 15 GHz. *Top:* images of the CLEAN model convolved with the natural restoring beam, with a mask applied for 8.4 GHz (*left*) and 15 GHz (*right*). Including the eastern jet emission resulted in a small nonphysical shift. Hence a mask was used to cut out the whole eastern jet and to only account for the emission of the western jet for the alignment. *Bottom:* contour maps without (*left*) and with applied shift (*right*).

Table 3. Shifts of frequency pairs resulting from 2D cross-correlation on optically thin regions.

ν_{low} [GHz]	ν_{high} [GHz]	RA [mas]	Dec [mas]
1.5	5.0	-3.920	3.360
5.0	8.4	-1.080	0.720
8.4	15	-0.450	0.000
15	22	-0.450	0.375
22	43	0.152	0.076

tion of a surrounding torus has a strong impact on the innermost region at frequencies below 43 GHz. For the cross-correlation, these areas have to be excluded to align only on optically thin structures. To account for this, we applied a mask to remove the obvious optically thick regions during the cross-correlation process. Figure 5 shows the alignment. The upper panels show the re-gridded and blurred images at 8 GHz and 15 GHz with an elliptical mask applied. In the lower panels, the contours of both maps are plotted without shift (*left*) and shifted according to the alignment (*right*). The derived pairwise shifts are listed in Table 3.

Previous observations of NGC 1052 revealed highly inverted spectral indices at the location of the emission gap between both jet bases, exceeding a spectral index of $\alpha = 2.5$ (where $S_\nu \propto \nu^\alpha$), which is explained by the obscuring torus resulting in free-free absorption. The same is observed for our new VLBA observations. Figure 6 shows a spectral index map derived from the 8 and 15 GHz images. Perpendicular to the jet axis, the distribution of spectral indices is smooth and consistent with previous observations, which is evidence that our alignment is correct. The same holds for the other frequency pairs.

Based on these shifts, all images have been aligned with respect to the 43 GHz image. This approach assumes the

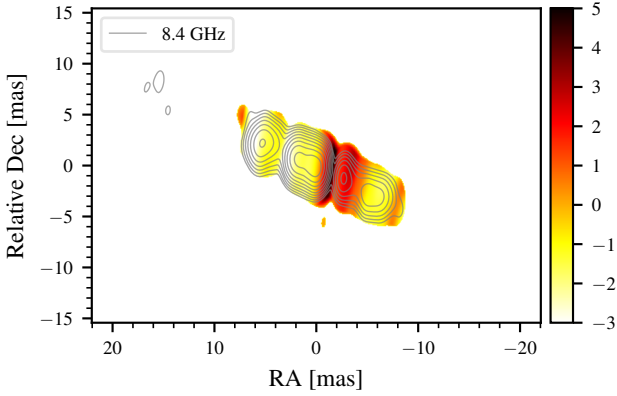


Fig. 6. Spectral index map between 8.4 GHz and 15 GHz. The contours in the maps correspond to the lower frequency of the pair and start at three times the noise level.

brightest component at 43 GHz to be the dynamic centre of the source following [Baczko et al. \(2019\)](#). These shifted images are used throughout the entire analysis when comparing the properties of the jets at different frequencies.

3.2. The ridge line in NGC 1052

To derive the ridge line that connects the local flux density maxima along both jets, for each image we followed the subsequent steps for each frequency using the naturally weighted images that detect the outer jet structures with a high S/N: (1) The images were restored with a circular beam of diameter $b = \sqrt{b_{\text{maj}} \times b_{\text{min}}}$ which maintains the beam area. All following procedures were run by a ParselTongue script (i.e. using AIPS tasks): (2) The images were rotated by 24° to align the main jet axis with the x -axis using the task LGEOM; (3) These images were sliced perpendicular to the jet axis at each pixel with the task SLICE; (4) One Gaussian was fitted to the slices with SLFIT. From these fits, we obtained the ridge line as well as the jet width (equal to the deconvolved full width at half maximum (FWHM) of the fitted slices) and peak flux density along the ridge line. We include only fits with (i) a FWHM larger than the circular beam size and (ii) a peak flux density higher than three times the noise level. The ridge line is plotted on top of the clean images in Figs. 1 and 3. The uncertainty on the deconvolved FWHM is estimated to be a combination of the error propagation of the fitting error and the imaging error, which we assumed to be one-tenth of the beam size (cf. [Park et al. 2021](#)). This is reasonable because of the high dynamic range of our images and the limitation to width measurement with a $S/N \geq 3$. The uncertainty on the apparent opening angle was derived by error propagation.

In Fig. 7 we compare jet width (top), peak flux density (middle top), apparent opening angle (middle bottom), and residuals (bottom) for all single-epoch observations for the eastern jet (left) and western counter-jet (right). The ridge lines were shifted according to Sect. 3.1 with respect to the 43 GHz image. We assumed the same shift for both 22 GHz observations from the VLBA and RadioAstron. The width and apparent opening angle as derived from the three stacked images are shown in Fig. 8. To examine the collimation profiles we fitted power laws to the jet width with distance. A first test fit of a single power law to both jets shows several deviations of the data from the model (compare Fig. 9). At distances closer than $\sim 10^4 R_S$, the fitted power law with index $k = 1.05 \pm 0.03$ does not describe the measured width. Given this clear deviation from a single power law, we fit

the data with a broken power-law model (see e.g. [Nakahara et al. 2020](#)):

$$w(z) = W_0 2^{(k_u - k_d)/s} \left(\frac{z}{z_b}\right)^{k_u} \left[1 + \left(\frac{z}{z_b}\right)^s\right]^{(k_d - k_u)/s}. \quad (1)$$

Here, W_0 is the width at the break point, $k_{u/d}$ are the power-law indices for the upstream and downstream parts ($w \propto z^k$) of the jet, that is, between dynamic centre and break point and beyond the break point, respectively, and z_b is the break location. The parameter s allows us to define the degree of sharpness. The fitting revealed no significant dependence of the results on sharpness for values between 10 and 100 for this parameter. In order to compare our results to [Nakahara et al. \(2020\)](#) we fixed s to a value of 10.

In addition, the residuals in the lower panel of Fig. 9 clearly indicate differences between the eastern and western jets. Whereas the western jet at distances $> 10^4 R_S$ is fitted well, the eastern jet would require a steeper gradient of around $k \sim 1.2$. Hence, in the following we only discuss our results based on broken power-law fits to both jets individually. The fitting results are listed in Tables 4 and 5.

4. Discussion

4.1. Collimation profiles

In order to study the collimation profile of the jets in NGC 1052 we fitted a broken power law to the width along both jets individually, as described in Sect. 3.2 (cf. Fig. 7). Assessing the goodness of the fit is difficult for a number of reasons. First of all, the fitted model is non-linear. Moreover, as we took measurements of the width of the jet in each pixel, which is smaller than the beam size, neighbouring measurements are likely correlated. Hence, the reduced χ^2 does not provide a reliable method for estimating the goodness of the fit. Therefore, we assess the residuals, plotted in the bottom panel of Fig. 7, to evaluate the goodness of the fit. Based on this approach we favour the broken power law. The single power law shows a clear discrepancy with the data points from the fit at distances < 2 mas from the centre (cf. Fig. 9 as an example for a single power-law fit to both jets).

We also cross-checked the smoothly broken power-law fit with the following procedure. For both jets, we generated 10^4 random break points along the entire jet length drawn from all frequencies. For each break point, we applied a single power-law fit in the inner and outer jet region. After all runs, we applied quality filters for the fits $0.8 \leq \chi^2_{\text{red}} \leq 3$ and prohibited cases where the inner or outer region would be fitted with more than 80% of the data along the jet length. From the remaining fits, we calculated the median and the mean for both jets (see Table 6), which is consistent with the findings for the smoothly broken power law.

There are significant differences between the eastern and western jets, especially at 1.5 GHz and 5 GHz. Therefore, we only discuss our results from fitting the width of each jet individually. Downstream of the break point at around $10^4 R_S$, the jets become almost conical. Upstream, they are close to cylindrical with a power-law index of $k_u \sim 0.17$. This kind of break in the collimation profile has been found for a number of (mostly one-sided) AGN jets. This includes low-luminosity AGN such as M 87 and 3C84, as well as high-luminosity radio galaxies such as Cygnus A. Assuming that the jet phenomenon is indeed universal, we expect to observe a similar behaviour for AGN jets with different radio powers. This makes a comparison of NGC 1052 to

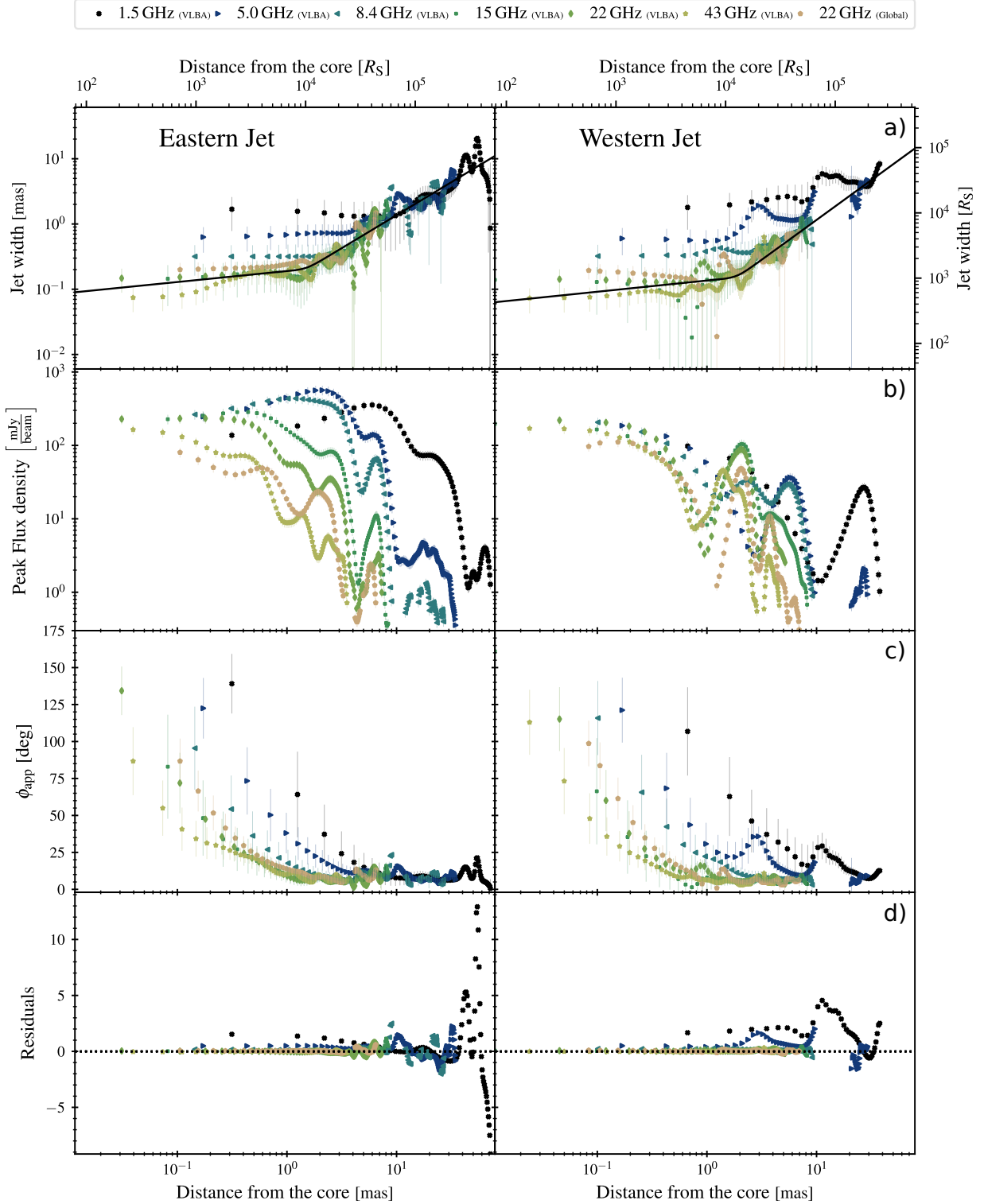


Fig. 7. Jet parameters obtained from the ridge line fitting of the Global and VLBA images. (a) Jet width, (b) peak flux density, (c) apparent opening angle, and (d) residuals of the data with the best fit along the jet ridge lines. Error bars are derived from a linear combination of the fitting and imaging error and are only plotted if exceeding the marker size. The values of R_S are computed assuming a black hole mass of $10^{8.2} M_\odot$.

other low-power and high-power sources extremely valuable for our understanding of the underlying physical processes behind the formation and collimation of jets at all scales.

For ten sources in the MOJAVE 15 GHz sample, Kovalev et al. (2020) found a break point in a typical range of $r_{\text{break}} \in (10^5, 10^6) r_S$, at which the shape changes from parabolic to conical. The same region was found in a few

single-source studies, including NGC 6251 (Tseng et al. 2016) and M 87 (Kim et al. 2018). Within this comparison, NGC 1052 stands out by not showing a parabolic expansion. One of the very few other sources with a similar cylindrical geometry is 3C 84 with a collimation profile of $r \propto z^{0.17 \pm 0.08}$ at distances of $180 R_S < z < 8000 R_S$, measured with RadioAstron (Giovannini et al. 2018). The findings of Nagai et al. (2014)

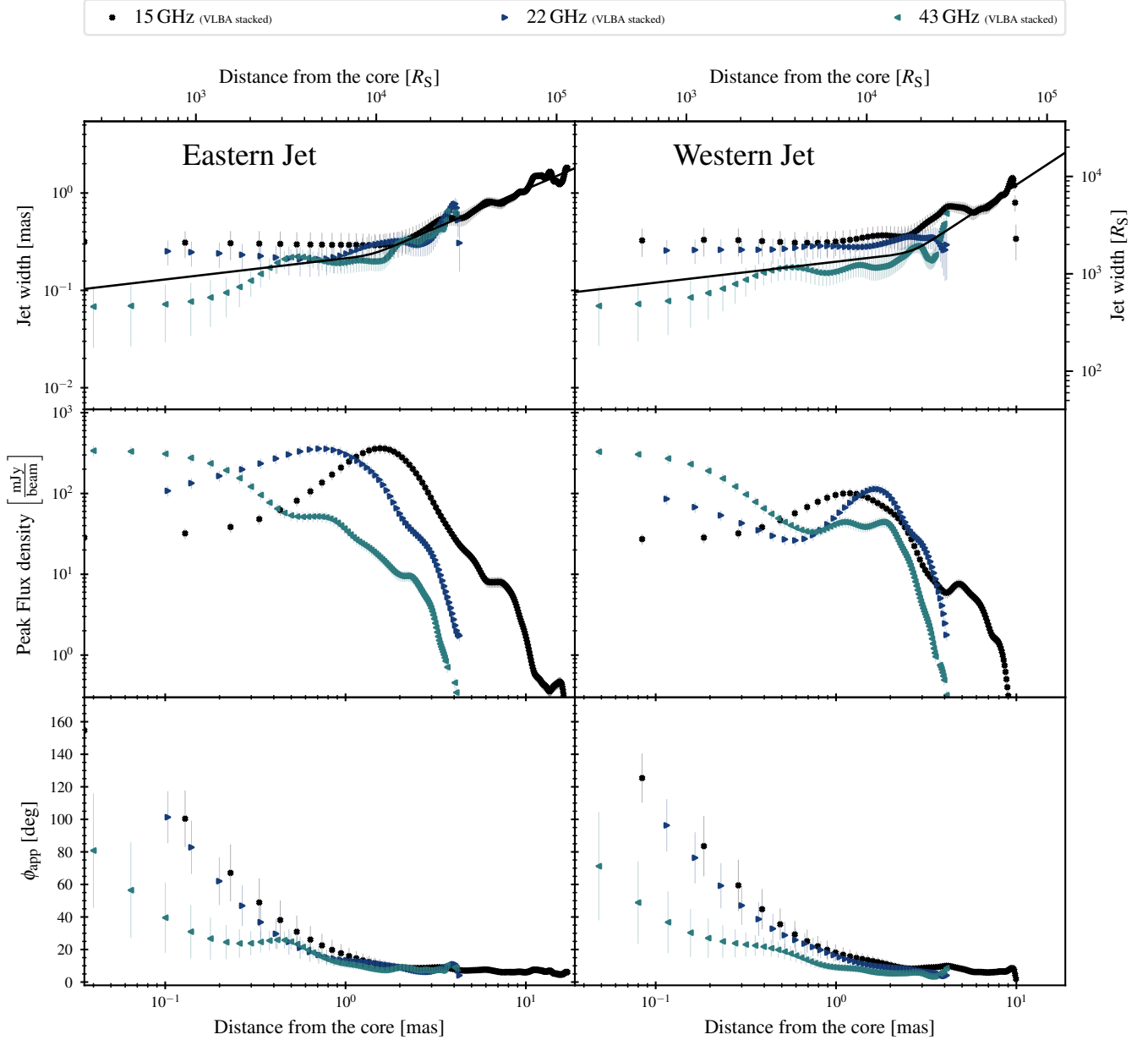


Fig. 8. Jet parameters obtained from the ridge line fitting of the stacked 15 GHz, 22 GHz, and 43 GHz VLBA images. *Top:* jet width. *Middle:* peak flux density. *Bottom:* apparent opening angle along the jet ridge lines. Error bars are derived from a linear combination of the fitting and imaging error and are only plotted if exceeding the marker size. The values of R_S are computed assuming a black hole mass of $10^{8.2} M_\odot$.

support a cylindrical profile down to at least $5 \times 10^4 R_S$ for this source. Similar wide but parabolic evolving jet bases are found in Cyg A with a minimum jet width of $227 \pm 98 R_S$ (Boccardi et al. 2016a). In Sect. 4.6, we further discuss the impacts of these findings on the collimation and acceleration zone.

The low-frequency data in the western jet are not consistent with a power law as the width is not simply decreasing upstream of the jet, but follows a step pattern. This cannot be observed in the eastern jet. We can exclude that this is due to an artefact of our analysis, as the slice profile clearly shows one peak and is fitted accurately with a single Gaussian. A similar larger width was also found by Nakahara et al. (2020) for the western jet. We therefore assume that this is a common feature observable in NGC 1052 and not due to the morphology of the source at the time of the observation. Assum-

ing this effect is not intrinsic to the jet, interaction with the surrounding medium is a likely explanation. Several authors found a dense plasma torus which covers larger parts of the western jet with respect to the eastern jet (see e.g. Kameno et al. 2001; Kadler et al. 2004a; Sawada-Satoh et al. 2008). Coinciding with the torus, H_2O maser emission was found (see e.g. Claussen et al. 1998). In addition, recent ALMA observations at submm wavelengths found a massive molecular torus with $M_{\text{torus}} = (1.3 \pm 0.3) \times 10^7 M_\odot$ inside a gas-poor circumnuclear disk (Kameno et al. 2020); with a radius of 2.4 ± 1.3 pc and a thickness ratio of 0.7 ± 0.3 , it covers the part of the western jet with deviating width measurements. Previous observations already connect the excess of absorption in between the jet cores with free-free absorption in a surrounding plasma torus (Kameno et al. 2001). With increasing observing frequency, its impact gets smaller and at around 43 GHz is almost negligible

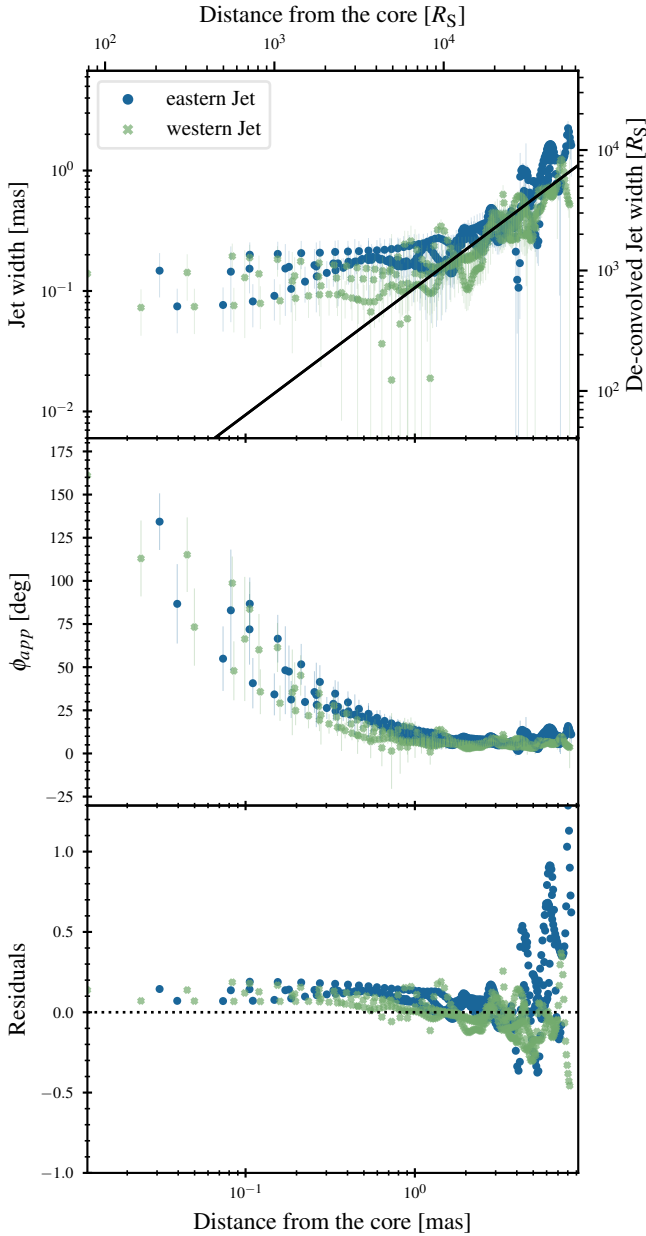


Fig. 9. Jet parameters obtained from the ridge line fitting of the Global 22 GHz and VLBA 15, 22, and 43 GHz images. *Top:* jet width, (*middle*) apparent opening angle, and (*bottom*) residuals of the data with the best fit along the jet ridge lines for both jets. The black line in the upper panel shows the best fit for a single power law. Error bars are derived from the fitting error and imaging error of one-tenth of the beam size and are only plotted if exceeding the marker size. The values of R_S are computed assuming a black hole mass of $10^{8.2} M_\odot$.

(Baczko et al. 2019). This absorption effect is larger for the western jet. With respect to the molecular torus, we may not only expect absorption but also scattering of the jet emission. As both effects are frequency dependent, this explains the large deviation of the widths at $\nu < 15$ GHz from a power law. To exclude this effect, we further focus on the collimation profile derived from our images with observing frequencies ≥ 15 GHz. The corresponding best-fit result is shown in Fig. 10 and Table 7.

The residuals still show deviations at larger distances. However, their amplitude is smaller and they spread symmetrically

Table 4. Fitting results from a broken power-law fit to the jet width at all frequencies for the single-epoch VLBA and RadioAstron observations.

Fit to	W_0	k_u	k_d	z_b [mas]
Eastern jet	0.21 ± 0.02	0.17 ± 0.09	1.01 ± 0.01	1.51 ± 0.19
Western jet	0.16 ± 0.01	0.17 ± 0.06	1.22 ± 0.02	1.88 ± 0.15
Both jets	0.19 ± 0.02	0.18 ± 0.06	1.11 ± 0.01	1.73 ± 0.14

Table 5. Fitting results from a broken power-law fit to stacked 15, 22, and 43 GHz VLBA images.

Fit to	W_0	k_u	k_d	z_b [mas]
Eastern jet	0.24 ± 0.02	0.22 ± 0.06	0.80 ± 0.01	1.40 ± 0.18
Western jet	0.26 ± 0.02	0.21 ± 0.05	1.22 ± 0.05	2.66 ± 0.22
Both jets	0.24 ± 0.02	0.20 ± 0.05	0.90 ± 0.01	1.79 ± 0.15

Table 6. Collimation profile results from cross-checks.

Fit to	\bar{k}_u	k_u^{med}	\bar{k}_d	k_d^{med}	\bar{z}_b [mas]	z_b^{med} [mas]
Eastern jet	0.96	0.96	0.29	0.18	1.77	1.12
Western jet	0.92	0.93	0.26	0.16	2.0	1.74

Table 7. Fitting results from a broken power-law fit to the jet width at frequencies ≥ 15 GHz.

Fit to	W_0	k_u	k_d	z_b [mas]
Eastern jet	0.35 ± 0.02	0.36 ± 0.05	1.76 ± 0.12	3.30 ± 0.24
Western jet	0.16 ± 0.01	0.16 ± 0.06	1.17 ± 0.04	1.78 ± 0.17
Both jets	0.32 ± 0.02	0.42 ± 0.04	1.70 ± 0.09	3.45 ± 0.19

around zero. Due to the absorbing effect of the surrounding torus, our data are sparse upstream of the break point and contain larger uncertainties in the western jet. There are now significant differences between the respective power laws of the eastern and western jets. In the approaching, eastern jet the break point of 3.3 mas and the upstream power-law index of $k_u = 0.36 \pm 0.05$ are consistent with the findings of Kovalev et al. (2020), whose measurements are based on 15 GHz VLBA data from the eastern jet. As the break point is found to be relatively far outside, the downstream power-law index is fitted with higher accuracy using all frequencies. Hence, from Table 4 and Fig. 7 this results in a downstream power-law index for the eastern jet of $k_d = 1.01 \pm 0.01$. The western jet changes from a more collimated jet to a conical expansion at a closer distance of 1.8 mas.

Further, our results are comparable to the findings by Nakahara et al. (2020) who derived the collimation parameters together for both jets based on archival observations. However, their work suggests a flatter profile close to $k_u = 0$. In addition, they did not find differences between the two jets, but suggest a symmetrical evolution. This discrepancy may be explained by the higher sensitivity of our data set in comparison to the older, archival data which were obtained in 2000 and 2001. Multi-epoch VLBA data at 43 GHz revealed changes in the morphology of the source within four years, being symmetrical in the beginning, and developing an asymmetric structure within one year. This resulted in the western counter-jet being brighter than the eastern jet (Baczko et al. 2019). Therefore, it cannot be

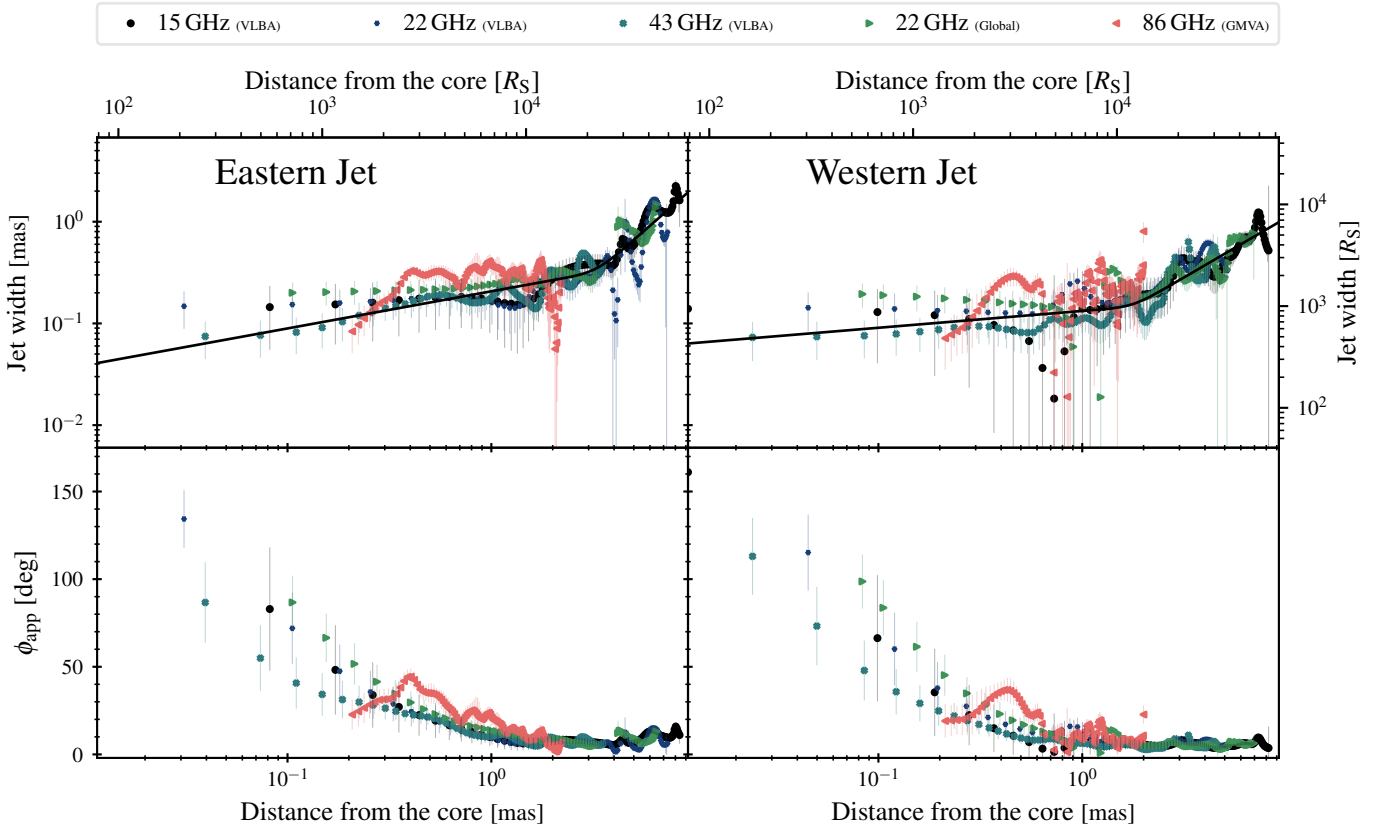


Fig. 10. Jet parameters obtained from the ridge line fitting of the Global 22 GHz and VLBA 15, 22, and 43 GHz images. Jet width (*top*) and apparent opening angle (*bottom*) along the jet ridge lines. The same parameters for the GMVA 86 GHz observation from 2004 are plotted on top, without being taken into account for the fit. Error bars are derived from a linear combination of the fitting and imaging error and are only plotted if exceeding the marker size. The values of R_S are computed assuming a black hole mass of $10^{8.2} M_\odot$.

excluded that the morphology – as well as the jet collimation – of the source in our observations is different from what is suggested by the data from 2001.

To study whether these differences between the two jets are a common feature or specific at this time of observation, in the following we discuss the outcomes from fitting the stacked VLBA images at 15, 22, and 43 GHz. In comparison to the higher frequency single-epoch images (Fig. 10), the fitting to the stacked images (Fig. 8) reveals consistent results for both jets, with a close-to cylindrical upstream power-law index of $k_u = 0.21$ and a conical downstream power-law index of $k_d = 0.80$ and $k_d = 1.22$ for the eastern and western jets, respectively. The widths of the western jet at 22 GHz and 15 GHz are slightly greater than those of the eastern jet. This points towards scattering at 15 GHz and 22 GHz in the western jet. In the eastern jet, the 15 GHz and 22 GHz widths upstream of $\sim 10^4 R_S$ do not decrease with decreasing distance to the core but follow a clear cylindrical profile. At distances closer than 0.3 mas, the widths measured at 43 GHz deviate from this and clearly decrease. Fitting only the width of the 43 GHz stacked image at distances $z < 2$ mas results in power-law indices of $k_u = 0.30 \pm 0.03$ and $k_u = 0.22 \pm 0.02$ for the eastern and western jets, respectively, which is similar to the fitting results obtained for the single-epoch observations. This difference between 43 GHz and lower frequencies suggests that different layers of the jet may be responsible for the emission at the individual frequencies. In Sect. 4.6 we briefly discuss the possibility of differential expansion.

4.2. The advantage of stacked images

Previous findings on the collimation profile of the jets in NGC 1052 are controversial. While multi-frequency but single-epoch observations found a cylindrical collimation profile with $k_u = 0$ upstream of $10^4 R_S$ (Nakahara et al. 2020), the power-law index based on a 15 GHz stacked image is, with $k_u = 0.391 \pm 0.048$, closer to a parabolic shape (Kovalev et al. 2020). On the one hand, Kovalev et al. (2020) only analysed the profile for the approaching jet and therefore the symmetry of the source was not studied. On the other hand, Nakahara et al. (2020) found both jets to be symmetric within errors; although the sampling of width measurements upstream of the break point is sparse and the broken power-law fit is largely guided by large-scale structures.

In our analysis we include the same VLBA 15 GHz images as Kovalev et al. (2020), applying a slightly different approach for alignment. Whereas the stacked images used in Kovalev et al. (2020) are aligned on the VLBI core, we shifted all images about the centre of the emission gap between both cores, where the 43 GHz core is assumed to reside (Baczko et al. 2019). This allows us to make a combined analysis of the 15, 22, and 43 GHz stacked images. Furthermore, the multi-frequency VLBA observations presented here are of improved sensitivity in comparison to the observations used by Nakahara et al. (2020), which were obtained more than ten years earlier. This results in detection of fainter jet emission in the outer parts of the jets and therefore in more pronounced differences between both jets.

With upstream power-law indices of $0.16 \leq k_u \leq 0.35$, we cannot confirm a truly cylindrical profile as proposed by

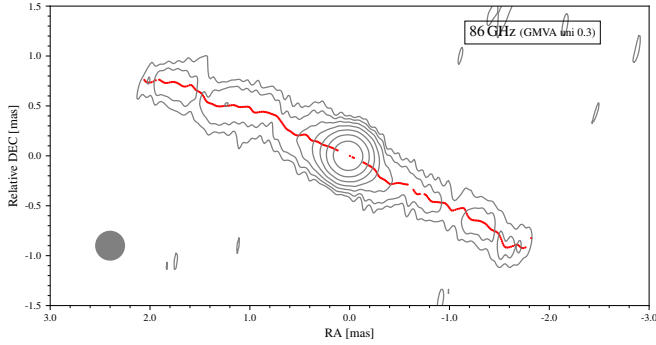


Fig. 11. Uniform weighted GMVA image from 2004 restored with a circular Gaussian of 0.3 mas (Baczko et al. 2016).

Nakahara et al. (2020), but taking into account only observations at frequencies $\nu \geq 15$ GHz, the power-law profile of the approaching, eastern jet is consistent with the findings of Kovalev et al. (2020). However, the stacked 43 GHz width profile indicates a more complicated structure, with a conical profile at $z \geq 10^4 R_S$, a cylindrical profile at $3 \times 10^3 R_S \leq z \leq 10^4 R_S$, and a quasi-parabolic profile at $z \leq 3 \times 10^3 R_S$.

A comprehensive study of multi-epoch 43 GHz observations of NGC 1052 revealed a dramatic change of the source morphology from being symmetric to asymmetric within timescales of about one year (Baczko et al. 2019). This suggests intrinsic asymmetric ejection of jet plasma into both the approaching and receding jets. As a consequence, the collimation profile might change depending on the observation date. This could explain the discrepancy between our multi-epoch observations and the findings by Nakahara et al. (2020). These temporal asymmetries of single-epoch observations make studies of jet collimation difficult. In contrast, our results from the multi-frequency stacked images suggest that the averaging allows us to measure the width of the whole jet channel, and therefore the true collimation profile, which can be connected to physical models of jet formation. Hence, in the case of NGC 1052, these kinds of studies have to be made with stacked images, especially at higher frequencies, to ensure that the whole jet channel is included in the analysis. Only then can reliable statements about the large-scale jet physics be made.

4.3. Comparison to 86 GHz GMVA observations

In order to ascertain the true collimation profile upstream of the break point and to exclude the effect of absorption and scattering, higher frequency images are needed, which suffer less from the surrounding plasma and molecular torus. The only detection of the jets at 86 GHz so far is from a GMVA observation from 2004 (Baczko et al. 2016). Given the 13 years between both observations and the close distance of this region to the central engine, those data are not included in the fitting, as this would require the assumption that no substantial changes took place over that interval. To still compare our results with the high-resolution image from 2004, we applied our ridge-line analysis to the archival data. We convolved the 86 GHz uniform weighted image with a circular beam of 0.3 mas, which is slightly smaller than the major axis of the beam (see restored image in Fig. 11).

The very elliptical beam produces non-physical, knotty structures perpendicular to the jet axis, if taking $b = \sqrt{b_{\text{maj}} \times b_{\text{min}}}$, as defined in Sect. 3.2. We assumed the 86 GHz centre to be located at the same position as the 43 GHz centre

and plotted the measurements on top of the higher frequency results in Fig. 10. We did not include the GMVA widths in the fit. The 2004 GMVA image has a gap between the innermost, unresolved bright component and the two jets, which have significant emission at distances $z > 0.2$ mas. Hence, we only include width measurements of both jets at these larger distances. Despite the 13-year difference between the two observations, the 86 GHz widths fit remarkably well to the power-law fits. Although the jets are only detected from 0.2 mas distances outwards, we can still compare the collimation profile with the upper limit on the size of the unresolved central 86 GHz core of $150 \mu\text{as}$ ($\sim 1000 R_S$) (Baczko et al. 2016). This value is consistent with the widths of the jets at the break point. Given that this is an upper limit, we cannot draw further conclusions about whether the jets continue with a close-to cylindrical profile down to the jet base or transition into a parabolic expansion at closer distance. In order to estimate the initial opening angle and the collimation at distances closer than $10^3 R_S$, higher sensitivity observations with a higher north–south resolution are decisive.

4.4. Apparent opening angle

Downstream of the break point, the jet is well collimated with a full apparent opening angle of $\phi_{\text{app}} < 10^\circ$. As before for the collimation profile, the western jet deviates from the overall trend at larger distances and at lower frequencies, being inconsistent with the assumption of a collimated outflow. In both jets, the apparent opening angle upstream of the break increases approaching the centre. However, with increasing observing frequency, the apparent opening angle decreases, being smallest at 43 GHz. Assuming that the image at 43 GHz is less affected by absorption and offers the highest resolution, it should provide the most accurate measurement of the innermost jet opening angle and jet width. As the central region is unresolved, we exclude measurements at distances $z < 0.15$ mas, which is equivalent to half the restored, circular beam at this frequency. This leads to an apparent opening angle at a distance of 0.15 mas of $\phi_{\text{app}} \sim 30^\circ$ for both jets. Taking into account a viewing angle of $i > 80^\circ$, the intrinsic opening angle is given by $\phi_{\text{intr}} = 2 \arctan(\sin i \tan(\phi_{\text{app}}/2))$ (Pushkarev et al. 2017). Based on the large viewing angle, the intrinsic angle, with $\phi_{\text{intr}} \geq 29.6^\circ$, is nearly identical to ϕ_{app} .

4.5. The straightness of the jets

Figure 12 shows all ridge lines at frequencies of $\nu \geq 15$ GHz plotted on top of each other. The ridge lines are found to be exceptionally straight at all scales over the whole set of observing frequencies. This is remarkable in comparison to other AGN sources. Many radio galaxies, such as Cyg A and 3C 84, have wide jet bases and are edge-brightened down to the closest measurable distances to the central engine (see e.g. Giovannini et al. 2018; Boccardi et al. 2016a). Bends and more complicated structures are a common feature observed for other AGN sources (e.g. CTA 102, 3C 345, PKS 0735+178 Fromm et al. 2013; Agudo et al. 2006; Pötzl et al. 2021). Kinematic studies of NGC 1052 revealed higher velocities at 43 GHz ($\beta \sim 0.5$) (Baczko et al. 2019) than at 15 GHz ($\beta \sim 0.2$) (Lister et al. 2019). Assuming that we observe an inner, faster layer of the jets at higher frequencies, this suggests jet stratification. This could be explained by assuming that the outer, slower moving layer consists of less energetic particles which are not emitting at 43 GHz and are therefore invisible. However, jet stratification is not visible in either the jet morphology or

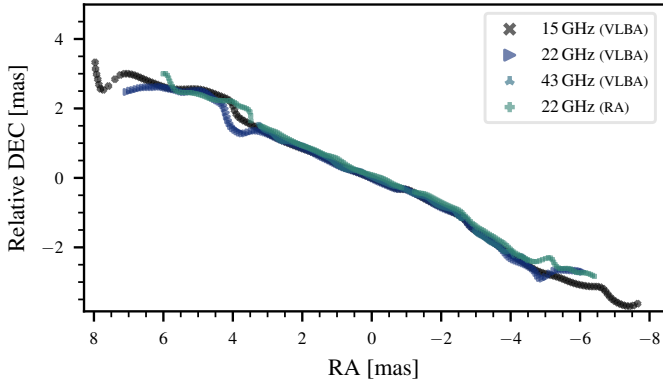


Fig. 12. Jet ridge lines compared for Global 22 GHz and VLBA 15, 22, 43 GHz observations.

the spectral index distribution. This non-detection of an edge-brightened structure might very well be explained by insufficient resolution. For example, the edge-brightened structure in Centaurus A was first discovered at the highest possible resolution obtained with the EHT (Janssen et al. 2021) and was not observable at lower frequencies.

There is one feature common to all images, which deviates slightly from the overall straight jet evolution. At -2.5 mas, the western jet changes its direction slightly towards the south to change back to the original position angle at -5 mas. There is nothing comparable in the eastern jet. This directional change coincides with the location of the break point in the collimation profile. In accordance with the previous section, we assume this not to be intrinsic to the jet plasma, but to be an effect of the surrounding ionised plasma. A similar, slight jet bending in the proximity of the break is also observed in 43 GHz images of Cyg A (Boccardi et al. 2016b).

4.6. The collimation and acceleration zone

The break of the broken power-law fit in both jets is located at around $10^4 R_S$ with a width at this location of ~ 0.2 mas. This is about two orders of magnitude closer than the sphere of gravitational influence (Sol) $R_{\text{Sol}} = 9.6 \times 10^5 R_S$ for NGC 1052 (Kameno et al. 2020). Hence, as the break location is clearly independent of the black hole influence, there remain two main mechanisms that can explain the observed jet properties.

First, as suggested by numerical simulations and observational considerations, the break most likely marks the position at which the jet transitions from being magnetically dominated to particle-dominated (Potter & Cotter 2015; Komissarov et al. 2009; Kovalev et al. 2020). However, it has been claimed that magnetic collimation is not the main collimation mechanism in extragalactic jets, as it would imply a strong toroidal magnetic field, which would make the jet very unstable (Mizuno et al. 2009, 2012; Perucho et al. 2017; Perucho 2019, and references therein). This is in clear contrast to the exceptional straightness of the jets.

Secondly, the geometric transition might result from a confinement of the jet through an external pressure profile (Lyubarsky 2009; Beskin et al. 2017; Kovalev et al. 2020). The complex inner structure of NGC 1052 is in favour of this explanation. NGC 1052 is surrounded by an optically thick plasma torus which covers the inner ~ 2 mas around the nucleus (Sawada-Satoh et al. 2008; Kameno et al. 2001) and a massive molecular torus inside a gas-poor circumnuclear disk

(Kameno et al. 2020). The outer extent of the plasma torus is in agreement with the location of the break in the collimation profile. In addition, NGC 1052 most likely hosts an advection-dominated accretion flow (ADAF) inside an optically thick, geometrically thin accretion disk, which is truncated at a distance of $r_{\text{tr}} \geq 13 R_S$ (Reb et al. 2018; Falocco et al. 2020). This might explain the atypical close-to-cylindrical collimation profile.

In addition, following Globus & Levinson (2016), collimation through a disk wind could also take place, which requires relatively large wind powers. On the other hand, emission from the disk wind itself might contribute to the imaged radiation, which has the potential to prevent us from detecting the true, intrinsic jet structure. Furthermore, deviations of the apparent opening angle and width with frequency upstream of the break point can be explained by differential expansion, which is required by magnetic acceleration (Vlahakis & Königl 2004; Komissarov et al. 2009; Komissarov 2012; Anglés-Castillo et al. 2021). Therefore, as we identify the region of differential expansion with the upstream jets at distances $\lesssim 10^4 R_S$, we expect the jet acceleration to take place in that region. Indeed, Fig. 6 of Baczko et al. (2019) shows some indication of flow acceleration within these inner 2 mas in both jets. This is most evident in the western jet components wj5, wj6, wj9, wj10, and wj12–15 and the eastern jet components ej3–5, ej12, and ej13 shown in this latter figure. Beyond this region, component trajectories are clearly linear, which coincides with the region in which the apparent opening angles merge for all observing frequencies within the present study. The observations presented are limited by resolution and absorption processes. To further investigate a possible differential expansion accompanied by acceleration, multi-epoch observations at frequencies > 43 GHz have to be conducted to perform detailed kinematic studies upstream of $10^4 R_S$.

In summary, external confinement and differential expansion are the most likely mechanisms driving the observed jet geometry in light of the deviation from a parabolic expansion and the possible jet acceleration upstream of the break point. It is especially interesting that, at 43 GHz, the profiles and opening angles are similar for the eastern and western jets. In contrast, the significant differences seen at lower frequencies make the double-sided jet system of NGC 1052 a very interesting target for further study of the impact of the surrounding material, such as that of the torus–accretion disk system, on the width measurement. This is not possible in one-sided jet sources. In addition, the width along both jets for the stacked 43 GHz image suggests an even more complex structure with a second break at around $3 \times 10^3 R_S$, which is more pronounced in the eastern jet. To further investigate this, higher sensitivity images at frequencies $\nu > 43$ GHz are required, which resolve structures closer to the black hole. With the high sensitivity of our multi-frequency and stacked images our results are the ideal starting point to study a possible jet collimation mechanism and the impact of a change in the outer pressure profile in greater detail by comparing with and guiding high-resolution 3D numerical simulations.

5. Summary

We present a detailed study of the ridge line and collimation profile of NGC 1052 over a frequency range from 1.5 GHz to 86 GHz observed with the VLBA and a large global array supporting a RadioAstron observation. Further, we compare the low radio power AGN NGC 1052 with powerful FR I and FR II

sources (e.g. 3C 84, M 87, and Cygnus A). The comparison between low- and high-power jets is extremely important for testing the universality of the jet phenomenon. Our main conclusions are summarised as follows:

- In accordance with previous observations we find a remarkably straight, low-velocity double-sided jet. There is no hint of any double ridge line depicting an edge-brightened structure as observed in other nearby AGN with highly relativistic jets, such as Cyg A, M 87, or 3C 84.
- There is a change from a nearly cylindrical to conical outflow at a break point of ~ 2 mas or $10^4 R_S$, which is slightly different for the eastern and western jets. This is much closer than the SoI of the black hole and we do not find any trace of a parabolic jet shape. NGC 1052 most likely hosts an ADAF inside a thin, truncated disk surrounded by a dense torus (Kamenov et al. 2001, 2020; Reb et al. 2018). This makes the most likely scenario one in which the jets are confined by an outer pressure gradient.
- At lower frequencies < 15 GHz there are significant differences between the eastern, approaching jet and the western, receding jet. On the one hand, the eastern jet is well described as displaying a conical expansion outside the break point over all frequencies. On the other hand, width measurements in the western jet at 1.5 GHz and 5 GHz deviate strongly from the conical expansion, showing a much wider jet as is expected, suggesting scattering from the dense molecular torus found by ALMA observations (Kamenov et al. 2020).
- Width measurements of archival 86 GHz data from 2004 are in agreement with the cylindrical jet shape upstream of the break point. However, the limited sensitivity and unresolved central component prevent us from drawing conclusions at distances $< 10^3 R_S$ to the central engine.
- With increasing frequency, the apparent opening angle decreases. In combination with a flow acceleration within the inner 2 mas, which is indicated in Fig. 6 in Baczko et al. (2019), this can be explained by differential expansion, which is required by magnetic acceleration. We do not detect an edge-brightened structure. This can be explained by insufficient resolution as is the case for Centaurus A, where edge-brightening could only be revealed with high-frequency observations with the EHT.
- At frequencies > 15 GHz, the single-epoch observations reveal significant differences between the eastern and western jets, which are not observed by Nakahara et al. (2020). However, by fitting stacked images, the upstream profile, with $k_u = 0.19$, is close to cylindrical for both jets and the downstream profiles are, with $k_u = 0.83$ and $k_u = 0.98$, close to conical for the eastern and western jets, respectively. This suggests that the full jet width can only be probed by stacked images. Still, the 15 GHz and 22 GHz stacked images reveal larger widths in the western jet in comparison to the eastern jet. Moreover, at distances < 0.2 mas the 43 GHz widths get smaller and their profiles of $k_u = 0.30 \pm 0.03$ and $k_u = 0.22 \pm 0.02$ for the eastern and western jets, respectively, deviate from the cylindrical profile observed at 15 and 22 GHz.

In order to investigate the jet shape upstream of the break point in more detail, high-frequency multi-epoch observations at frequencies ≥ 86 GHz with a higher north–south resolution will be decisive. The same holds for estimation of the initial opening angle.

Acknowledgements. The authors would like to thank the anonymous referee for his/her useful comments. We thank Michael Janssen for his valuable comments to the manuscript. We thank Gabriele Bruni, Mikhail Lisakov and Tuomas Savolainen for their strong support in the correlation of the RadioAstron observation. The RadioAstron project is led by the Astro Space Center of the Lebedev Physical Institute of the Russian Academy of Sciences and the Lavochkin Scientific and Production Association under a contract with the State Space Corporation ROSCOSMOS, in collaboration with partner organizations in Russia and other countries. Partly based on observations performed with radio telescopes of IAA RAS (Federal State Budget Scientific Organization Institute of Applied Astronomy of Russian Academy of Sciences). The European VLBI Network is a joint facility of independent European, African, Asian, and North American radio astronomy institutes. Partly based on observations with the 100-m telescope of the MPIfR (Max-Planck-Institut für Radioastronomie) at Effelsberg. Results of optical positioning measurements of the Spektr-R spacecraft by the global MASTER RoboticNet (Lipunov et al. 2010), ISON Collaboration, and Kourvka observatory were used for spacecraft orbit determination in addition to mission facilities. The National Radio Astronomy Observatory is a facility of the National Science Foundation operated under cooperative agreement by Associated Universities, Inc. The data were correlated at the DiFX correlator (Deller et al. 2011; Bruni et al. 2016) of the MPIfR at Bonn. This research has made use of NASA’s Astrophysics Data System. This research has made use of the NASA/IPAC Extragalactic Database (NED), which is operated by the Jet Propulsion Laboratory, California Institute of Technology, under contract with the National Aeronautics and Space Administration. This research has made use of Astropy, a community-developed core Python package for Astronomy (Astropy Collaboration 2013, 2018), the scikit-image bibliography (van der Walt et al. 2014), scipy (Jones et al. 2001), and the ODR package, based on Boggs & Rogers (1990). MP acknowledges support by the Spanish Ministry of Science through Grants PID2019-105510GB-C31, PID2019-107427GB-C33, and from the Generalitat Valenciana through grant PROMETEU/2019/071. CMF is supported by the black hole initiative at Harvard University, which is supported by a grant from the John Tempelton Foundation.

References

- Agudo, I., Gómez, J. L., Gabuzda, D. C., et al. 2006, *A&A*, **453**, 477
- Anglés-Castillo, A., Perucho, M., Martí, J. M., & Laing, R. A. 2021, *MNRAS*, **500**, 1512
- Asada, K., & Nakamura, M. 2012, *ApJ*, **745**, L28
- Astropy Collaboration (Robitaille, T. P., et al.) 2013, *A&A*, **558**, A33
- Astropy Collaboration (Price-Whelan, A. M., et al.) 2018, *AJ*, **156**, 123
- Baczko, A.-K., Schulz, R., Kadler, M., et al. 2016, *A&A*, **593**, A47
- Baczko, A. K., Schulz, R., Kadler, M., et al. 2019, *A&A*, **623**, A27
- Baloković, M., Cabral, S. E., Brenneman, L., & Urry, C. M. 2021, *ApJ*, **916**, 90
- Beskin, V. S., Chernoglazov, A. V., Kiselev, A. M., & Nokhrina, E. E. 2017, *MNRAS*, **472**, 3971
- Blandford, R. D., & Königl, A. 1979, *ApJ*, **232**, 34
- Blandford, R. D., & Payne, D. G. 1982, *MNRAS*, **199**, 883
- Blandford, R. D., & Znajek, R. L. 1977, *MNRAS*, **179**, 433
- Boccardi, B., Krichbaum, T. P., Bach, U., Bremer, M., & Zensus, J. A. 2016a, *A&A*, **588**, L9
- Boccardi, B., Krichbaum, T. P., Bach, U., et al. 2016b, *A&A*, **585**, A33
- Boccardi, B., Krichbaum, T. P., Ros, E., & Zensus, J. A. 2017, *A&ARv*, **25**, 4
- Boccardi, B., Perucho, M., Casadio, C., et al. 2021, *A&A*, **647**, A67
- Böck, M. 2012, PhD Thesis, Friedrich-Alexander-Universität Erlangen-Nürnberg
- Boggs, P. T., & Rogers, J. E. 1990, in *Statistical Analysis of Measurement Error Models and Applications: Proceedings of the AMS-IMS-SIAM Joint Summer Research Conference held June 10–16, 1989*, eds. P. Brown, & W. Fuller, (American Mathematical Society), *Contemp. Math. Ser.*, **112**, 186
- Brenneman, L. W., Weaver, K. A., Kadler, M., et al. 2009, *ApJ*, **698**, 528
- Bruni, G., Anderson, J., Alef, W., et al. 2016, *Galaxies*, **4**, 55
- Chael, A. A., Johnson, M. D., Narayan, R., et al. 2016, *ApJ*, **829**, 11
- Chael, A. A., Johnson, M. D., Bouman, K. L., et al. 2018, *ApJ*, **857**, 23
- Claussen, M. J., Diamond, P. J., Braatz, J. A., Wilson, A. S., & Henkel, C. 1998, *ApJ*, **500**, L129
- Deller, A. T., Brisken, W. F., Phillips, C. J., et al. 2011, *PASP*, **123**, 275
- EHT Collaboration (Akiyama, K., et al.) 2019, *ApJ*, **875**, L1
- Falocco, S., Larsson, J., & Nandi, S. 2020, *A&A*, **638**, A67
- Fosbury, R. A. E., Mebold, U., Goss, W. M., & Dopita, M. A. 1978, *MNRAS*, **183**, 549
- Fromm, C. M., Ros, E., Perucho, M., et al. 2013, *A&A*, **557**, A105
- Fromm, C. M., Perucho, M., Porth, O., et al. 2018, *A&A*, **609**, A80
- Fromm, C. M., Younsi, Z., Baczko, A., et al. 2019, *A&A*, **629**, A4
- Giovannini, G., Savolainen, T., Orienti, M., et al. 2018, *Nat. Astron.*, **2**, 472

- Globus, N., & Levinson, A. 2016, *MNRAS*, **461**, 2605
- Greisen, E. W. 1990, *Acquisition, Processing and Archiving of Astronomical Images*, 125
- Ho, L. C., Filippenko, A. V., & Sargent, W. L. W. 1997, *ApJS*, **112**, 315
- Janssen, M., Falcke, H., Kadler, M., et al. 2021, *Nat. Astron.*, **5**, 1017
- Jensen, J. B., Tonry, J. L., Barris, B. J., et al. 2003, *ApJ*, **583**, 712
- Jones, E., Oliphant, T., Peterson, P., et al. 2001, *SciPy: Open Source Scientific Tools for Python*, <http://www.scipy.org>
- Kadler, M., Kerp, J., Ros, E., et al. 2004a, *A&A*, **420**, 467
- Kadler, M., Ros, E., Lobanov, A. P., Falcke, H., & Zensus, J. A. 2004b, *A&A*, **426**, 481
- Kameno, S., Sawada-Satoh, S., Inoue, M., Shen, Z.-Q., & Wajima, K. 2001, *PASJ*, **53**, 169
- Kameno, S., Sawada-Satoh, S., Impellizzeri, C. M. V., et al. 2020, *ApJ*, **895**, 73
- Kardashev, N. S., Kovalev, Y. Y., & Kellermann, K. I. 2012, *The Radio Science Bulletin No. 343*, 343, 22
- Kettenis, M., van Langevelde, H. J., Reynolds, C., & Cotton, B. 2006, in *Astronomical Data Analysis Software and Systems XV*, eds. C. Gabriel, C. Arviset, D. Ponz, & S. Enrique, *ASP Conf. Ser.*, **351**, 497
- Kim, J. Y., Krichbaum, T. P., Lu, R. S., et al. 2018, *A&A*, **616**, A188
- Komissarov, S. S. 2012, *MNRAS*, **422**, 326
- Komissarov, S. S., Vlahakis, N., Königl, A., & Barkov, M. V. 2009, *MNRAS*, **394**, 1182
- Kovalev, Y. Y., Pushkarev, A. B., Nokhrina, E. E., et al. 2020, *MNRAS*, **495**, 3576
- Lipunov, V., Kornilov, V., Gorbvskoy, E., et al. 2010, *Adv. Astron.*, **2010**, 349171
- Lister, M. L., Homan, D. C., Hovatta, T., et al. 2019, *ApJ*, **874**, 43
- Lyubarsky, Y. 2009, *ApJ*, **698**, 1570
- Mizuno, Y., Lyubarsky, Y., Nishikawa, K.-I., & Hardee, P. E. 2009, *ApJ*, **700**, 684
- Mizuno, Y., Lyubarsky, Y., Nishikawa, K.-I., & Hardee, P. E. 2012, *ApJ*, **757**, 16
- Nagai, H., Haga, T., Giovannini, G., et al. 2014, *ApJ*, **785**, 53
- Nakahara, S., Doi, A., Murata, Y., et al. 2020, *AJ*, **159**, 14
- Park, J., Hada, K., Nakamura, M., et al. 2021, *ApJ*, **909**, 76
- Perucho, M. 2019, *Galaxies*, **7**, 70
- Perucho, M., Martí, J. M., Gómez, J. L., & Fuentes, A. 2017, *XII Multifrequency Behaviour of High Energy Cosmic Sources Workshop (MULTIF2017)*, 64
- Petrov, L., Kovalev, Y. Y., Fomalont, E. B., & Gordon, D. 2011, *AJ*, **142**, 35
- Potter, W. J., & Cotter, G. 2015, *MNRAS*, **453**, 4070
- Pötzl, F. M., Lobanov, A. P., Ros, E., et al. 2021, *A&A*, **648**, A82
- Pushkarev, A. B., Kovalev, Y. Y., Lister, M. L., & Savolainen, T. 2017, *MNRAS*, **468**, 4992
- Reb, L., Fernández-Ontiveros, J. A., Prieto, M. A., & Dolag, K. 2018, *MNRAS*, **478**, L122
- Sawada-Satoh, S., Kameno, S., Nakamura, K., et al. 2008, *ApJ*, **680**, 191
- Shepherd, M. C., Pearson, T. J., & Taylor, G. B. 1994, *BAAS*, **26**, 987
- Tseng, C.-Y., Asada, K., Nakamura, M., et al. 2016, *ApJ*, **833**, 288
- Tully, R. B., Courtois, H. M., Dolphin, A. E., et al. 2013, *AJ*, **146**, 86
- van der Walt, S., Schönberger, J. L., Nunez-Iglesias, J., et al. 2014, *PeerJ*, **2**, e453
- Vega-García, L., Lobanov, A. P., Perucho, M., et al. 2020, *A&A*, **641**, A40
- Vermeulen, R. C., Ros, E., Kellermann, K. I., et al. 2003, *A&A*, **401**, 113
- Vlahakis, N., & Königl, A. 2004, *ApJ*, **605**, 656
- Woo, J.-H., & Urry, C. M. 2002, *ApJ*, **579**, 530
- Zensus, J. A. 1997, *ARA&A*, **35**, 607